This is a repository copy of *Lattice Boltzmann simulation of flow past a spherical/non-spherical particle in a wide range of Reynolds number*.

Lattice Boltzmann simulation of flow past a spherical/non-spherical particle in a wide range of Reynolds number

Yanjun Guan[a,b], Rodrigo Guadarrama-Lara[b], Xiaodong Jia[b*], Kai Zhang[a*], Dongsheng Wen[b*]

（[a]Beijing Key Laboratory of Emission Surveillance and Control for Thermal Power Generation, North China Electric Power University, Beijing 102206, China

[b]School of Chemical and Process Engineering, University of Leeds, Leeds LS2 9JT, UK）

Corresponding author:

Xiaodong Jia; Tel: +44 (0)113 3432801; Email: X.Jia@leeds.ac.uk

Kai Zhang; Tel: +86 10 61772413; Email: kzhang@ncepu.edu.cn

Dongsheng Wen; Tel: +44 113 3431299; Email: d.wen@leeds.ac.uk

Highlights

Lattice Boltzmann method is used to determine the hydrodynamic force

Flow past a spherical particle in a wide range of Reynolds numbers

Flow past a non-spherical particle in a wide range of Reynolds numbers

Simulation results in good agreement with experimental data or empirical correlations

Abstract

Lattice Boltzmann method was used to predict the fluid-particle interaction for arbitrary shaped particles. In order to validate the reliability of the present approach, flow past a single stationary spherical, cylindrical or cubic particle is conducted in a wide range of Reynolds number ($0.1 < Re_p < 1000$). Simulated results indicate that the drag coefficient is closely related to the particle shape, especially at the high Reynolds number. The resolution of spherical particle plays a key role in accurately predicting the drag coefficient at high Reynolds numbers. For the non-spherical particle, the drag coefficient is more influenced by the particle morphology at moderate or high Reynolds numbers than at low ones. Good agreements between the simulated drag coefficient values and the experimental date or empirical correlations are achieved for both the spherical and non-spherical particles.

1. Introduction

The fluid-particle flow occurs widely in natural and industrial processes, such as dust and pollutant in air, sediment grains transport in rivers, gas/liquid-particle flows in chemical reactors and many others (Holzer and Sommerfeld, 2009; Ouchene et al., 2015). The comprehensive knowledge about the drag force on a single particle is essential for understanding the complexly physics of fluid-particle flow. Numerous efforts have been focused on the fluid drag on a spherical particle to obtain an appropriate correlation (Fair and Geyer, 1954; Haider and Levenspiel, 1989; Yow et al, 2005). Most of the experimental drag coefficient values were obtained by particle settling experiments at low Reynolds number and by wind tunnel experiments at high Reynolds number (Holzer and Sommerfeld, 2009). Several correlations for the spherical particle have been proposed in the literature with different accuracy and range of applicability (Brown and Lawler, 2003). Based on a critical review of the published data, Clift et al. (1978) proposed a correlation consists of 6 polynomial equations with 18 fitted constants. This correlation shows better goodness of fit to the 408 experimental data reported in the literature. Brown and Desmond (2003) reviewed the historical experimental efforts about the fluid dynamics drag on a spherical particle since the beginning of 20th century, and concluded that the correlation by Clift et al. (1978) is the best for drag coefficient for spheres, despite of the slight discontinuities at some transition points from one Reynolds number range to another.

A noteworthy fact is that non-spherical particles rather than perfect spheres are generally involved in practical fluid-particle systems. Such shape diversity adds difficulties in estimating the fluid-particle interaction (Rong et al., 2015). For the non-spherical particles, Holzer and Sommerfeld (2008) plotted the experimental drag

coefficients verse Reynolds numbers, for a number of different shapes including spheres, disks and plates, lengthwise spheroids and streamline bodies, isometric particles (e.g., cubes, tetrahedrons and octahedrons) and some irregular shaped particles. It was observed that the particle shape had a strong influence on the profile of drag coefficient. The correlations for spherical particle were not valid for the non-spherical particle since the drag coefficient was closely related to particle shape. Up to now, several drag correlations for non-spherical particles have been proposed from the experimental data (Haider and Levenspiel, 1989; Ganser, 1993; Holzer and Sommerfeld, 2008). Haider and Levenspiel (1989) proposed the first generalized correlation to associate the drag coefficient with the Reynolds number for spherical particle and non-spherical particle, the so-called sphericity was introduced to describe the effect of particle shape. Ganser (1993) assumed that each isolated particle experiences a Stokes's regime where drag was proportional to velocity and a Newton's regime where drag was proportional to the square of velocity, and then developed a correlation for both spherical and non-spherical particles containing the Stokes' shape factor and the Newton's shape factor. A simple correlation for the drag coefficient of an arbitrary shaped particle was established based on a large number of experimental data published in the literature (Holzer and Sommerfeld, 2008). The mean relative deviation between this correlation and 2061 experimental data for different shapes was 14.1%, which was much lower than that of 383% and 348% for correlations of Haider and Levenspiel (1989) and Ganser (1993), respectively. The commonly used correlations for spherical and non-spherical particles are list in Table1.

Table 1 Drag correlation for single particle

	Correlation

Clift et al. (1978)	$C_D = \dfrac{24}{Re} + \dfrac{3}{16}$, $\quad Re < 0.01$ $C_D = \dfrac{24}{Re}\left[1 + 0.1315 Re^{(0.82-0.05w)}\right]$, $\quad 0.01 \leq Re \leq 20$ $C_D = \dfrac{24}{Re}(1 + 0.935 Re^{0.6305})$, $\quad 20 \leq Re \leq 260$ $\log_{10} C_D = 1.6435 - 1.1242w + 0.1558w^2$, $\quad 260 \leq Re \leq 1500$ $\log_{10} C_D = -2.4571 + 2.5558w - 0.9295w^2 + 0.1049w^3$ $\quad\quad\quad 1500 \leq Re \leq 12000$ $\log_{10} C_D = -1.9181 + 0.6370w - 0.0636w^2$, $\quad 12000 \leq Re \leq 44000$ $\log_{10} C_D = -4.3390 + 1.5809w - 0.1546w^2$, $\quad 44000 \leq Re \leq 338000$ $w = \log_{10} Re$, ϕ is the sphericity
Haider and Levenspiel (1989)	$C_D = \dfrac{24}{Re}\left[1 + ARe^B\right] + \dfrac{C}{\left[1 + \dfrac{D}{Re}\right]}$ $A = \exp(2.3288 - 6.4581\phi + 2.4486\phi^2)$ $B = 0.0964 + 0.5565\phi$ $C = \exp(4.905 - 13.8944\phi + 18.4222\phi^2 - 10.2599\phi^3)$ $D = \exp(1.4681 + 12.2584\phi - 20.7322\phi^2 + 15.8855\phi^3)$ ϕ is the sphericity
Ganser (1993)	$\dfrac{C_D}{K_2} = \dfrac{24}{ReK_1K_2}\left[1 + 0.1118(ReK_1K_2)^{0.6567}\right] + \dfrac{0.4305}{1 + \dfrac{3305}{ReK_1K_2}}$ $K_1 = \left(\dfrac{1}{3} + \dfrac{2}{3}\phi^{(-\frac{1}{2})}\right)^{-1} - 2.25\dfrac{d_v}{D}$ for isometric shaped particle $K_1 = \left(\dfrac{1}{3}\dfrac{d_n}{d_v} + \dfrac{2}{3}\phi^{(-\frac{1}{2})}\right)^{-1} - 2.25\dfrac{d_v}{D}$ for nonisometric shaped particle $K_2 = 10^{1.8148(-\log_{10}\phi)^{0.5743}}$ ϕ is the sphericity
Holzer and Sommerfeld (2008)	$C_D = \dfrac{8}{Re}\dfrac{1}{\sqrt{\phi_\parallel}} + \dfrac{16}{Re}\dfrac{1}{\sqrt{\phi}} + \dfrac{3}{\sqrt{Re}}\dfrac{1}{\phi^{\frac{3}{4}}} + 0.421 0^{0.4(-\log\phi)^{0.2}}\dfrac{1}{\phi_\perp}$ $\phi_\parallel$ is the crosswise sphericity $\phi_\perp$ is the lengthwise sphericity

Numerical simulation is an effective alternative method for predicting the flow past a single particle. Most of these investigations were limited to low-to-moderate Reynolds numbers, based on the Finite Volume (FV) method. Johnson and Patel (1999) simulated the flow of incompressible viscous fluid past a sphere over flow regime for Reynolds number up to 300. Their numerical results showed good

agreement with the experimental observations. Bagchi et al. (2001) investigated the flow and heat transfer past a sphere in a uniform cross-flow for Reynolds numbers up to 500. Atefi et al. (2007) carried out computations to determine the fluid drag of 3-D flow past a stationary sphere at low and moderate Reynolds numbers in the range of 0.1~200. For the case of non-spherical particle, Dwyer and Dandy (1990) performed the simulations of flow past a non-spherical particle in a moderate Reynolds numbers range ($10 \leq Re_p \leq 66$), the effect of particle shape and orientation on the dynamics force and heat transfer characteristics were investigated in their study. Saha (2004, 2006) simulated the flow transition and heat transfer past a cube in Reynolds number range of 20~400. Valil and Green (2009) simulated the flow past two dimensional cylinders for Reynolds numbers in the range of 1~40, the effect of aspect ratios and inclination angle on the drag and lift coefficients were analyzed in their work. Richter and Nikrityuk (2013) investigated the dynamic force and heat transfer process for flow past ellipsoidal and cubic particles. On the other hand, the Lattice Boltzmann (LB) method was developed to calculate the fluid-particle hydrodynamics force by Ladd (1994a; 1994b). The most notable feature of LB method is that the computational cost scales linearly with the number of particles. In the past 20 years, the increasing efforts have been carried out on flow past single particle or arrays of particles (Peng and Luo, 2008; Holzer and Sommerfeld, 2009; Rong et al., 2013; Zhou and Fan, 2015). Peng and Luo (2008) simulated the steady and unsteady flows past a 2-dimensional circular cylinder with the Reynolds number of 20 and 100. Rong et al. (2009) investigated the flow past a sphere for Reynolds number up to 400. The drag, lift and torque for flow past a non-spherical particle was determined in the Reynolds number range of 0.3~240 by Holzer and Sommerfeld (2009). Although both the FV and LB methods have been applied to simulate the flow past a single spherical or non-spherical particle,

most of these investigations focused on the flow at low or moderate Reynolds numbers ($Re_p \leq 500$).

Discrete element method (DEM) has become an effective alternative to describe the movement of non-spherical particle. Several methods have been developed for modelling different shaped particles in DEM: composite particles, smooth and continuous surface particles, combined surface particles and digital particles (Favier et al., 1999; Jia and Williams, 2001; Jia et al., 2007; Wachs et al., 2012; Boon et al., 2013). Each method has its advantages and disadvantages in terms of accuracy, versatility, complexity and speed (Dong et al., 2015). In the investigations described in this series, DigiDEM coupled with LB method is used to simulate particle movements in fluidised beds. DigiDEM is an implementation of the DEM, but instead of spheres it uses voxels (3d pixels) to represent particles (Caulkin et al, 2009). The basic concept of this voxel based approach is that any shaped particle – including its internal structure, surface texture as well as the overall shape – can be represented by a coherent collection of voxels. The resolution depends on how accurate the shape needs in particular applications (Jia and Williams, 2001; Jia et al., 2007). Compared with other methods, the digital approach is not limited to mathematically easily describable shapes. The voxels are used to represent an arbitrary shaped particle; the computational cost is dependent on the total number of voxels and relatively independent of shape complexity. Since both DigiDEM and LB method operate on the same regular lattice grids, it is conceptually easy to couple the two, and the coupling has the potential for describing fluid-particle interactions better than existing methods for fluidised beds involving particles of arbitrary shapes. Accurate prediction of drag force on individual particle is fundamental in understanding the hydrodynamic behaviour of a fluidised bed. In order to validate the predictive ability of the program,

a LB implementation is tested over a much wider range of Reynolds number for different shapes in this study. The fluid drag acting on a particle is represented in terms of the drag coefficient. The influences of particle resolution, Reynolds number and particle shape on the drag coefficient are carefully analysed, and results compared with the experimental data and the empirical correlation published in the literature.

2. Mathematical model and numerical method

2.1. Lattice Boltzmann method

The LB method is originated from the Lattice Gas Automata (LGA). Compared to the traditional CFD method that solve the Navier-Stokes equation for the macroscopic fluid dynamics, i.e. pressure and velocity, the LB method can be used to simulate fluid flow in terms of the particle distribution function, which exist at each of the grid nodes that make up the fluid domain (Yu and Fan, 2010; Li et al., 2016). The particle distribution functions relate the probable amount of fluid particles moving with a discrete speed in a discrete direction at each lattice node at each time increment. The particle distribution functions are analogous to the continuous, microscopic density function of the Boltzmann equation. For the LB method, time and space coordinates are discretized with velocity range in phase space limited to a finite set of vectors that represent the directions in which the fluid particles can travel. The D3Q19 model is employed in this study, as shown in Fig. 1. It has 18 discrete lattice velocities with one fluid particle at rest. Components of D3Q19 lattice are listed in matrix as

$$\boldsymbol{c_i} = c \begin{bmatrix} 0 & 1 & -1 & 0 & 0 & 0 & 0 & 1 & -1 & -1 & 1 & 1 & -1 & -1 & 1 & 0 & 0 & 0 & 0 \\ 0 & 0 & 0 & 1 & -1 & 0 & 0 & 1 & 1 & -1 & -1 & 0 & 0 & 0 & 0 & 1 & -1 & -1 & 1 \\ 0 & 0 & 0 & 0 & 0 & 1 & -1 & 0 & 0 & 0 & 0 & 1 & 1 & -1 & 1 & 1 & 1 & -1 & -1 \end{bmatrix} \quad (1)$$
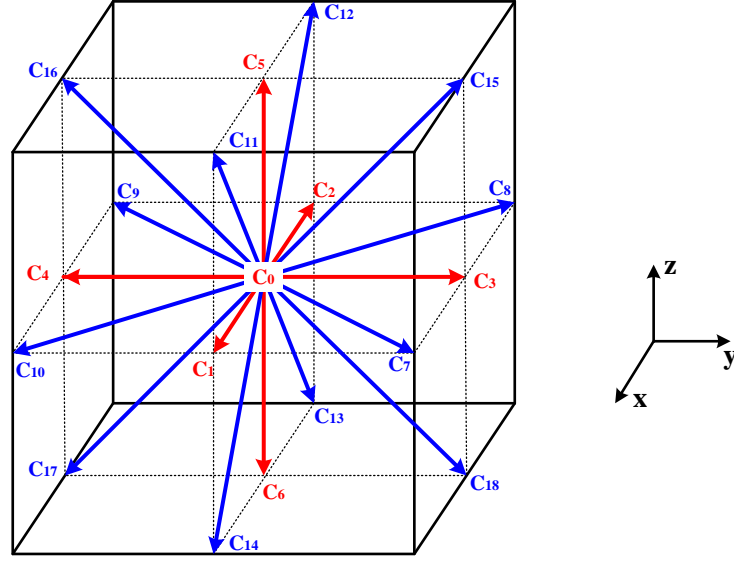
Fig. 1. Schematic of D3Q19 lattice

The basic LB method algorithm involves the streaming and collision processes at each node and each time step: streaming process propagates particle distribution function value between neighbour nodes (Eq. 2); collision process redistributes the functions that arrive at each node (Eq. 3), as expressed:

$$f_i(x + c_i\Delta t, t + \Delta t) = f_i^*(x,t) \tag{2}$$

$$f_i^*(x,t) = f_i(x,t) + \Omega_i(f(x,t)) \tag{3}$$

where Δx is the lattice spacing, Δt is the explicit time step, $f_i^*(x,t)$ and $f_i(x,t)$ are the post-collision and pre-collision distribution functions, respectively. $\Omega_i(f(x,t))$ is the collision operator, it controls the relaxation rate of particle distribution function.

Kinetic model: The relaxation process of the LB method acts on the non-equilibrium part of the distribution functions at a node to drive them towards equilibrium. By assuming that the collision operator relaxes the local particle distribution functions at a single rate it can be simplified to, in conjunction with an

appropriate equilibrium distribution function, the Bhatnagar-Gross-Krook (BGK) model was proposed by researchers, the collision term in BGK model is written as

$$\Omega_i(f(x,t)) = -\frac{1}{\tau}\left[f_i(x,t) - f_i^{(eq)}(x,t)\right] \tag{4}$$

here, τ is the relaxation time and it controls the rate at which the distribution functions tend toward equilibrium value, and fluid viscosity as follows

$$\nu = \frac{1}{3}\left(\tau - \frac{1}{2}\right)\frac{\Delta x^2}{\Delta t} \tag{5}$$

where Δx is the lattice spacing, Δt is the time increment, and the lattice speed is defined as $c = \Delta x/\Delta t$. $f_i^{(eq)}(x,t)$ is the equilibrium distribution function which is obtained from the macroscopic values of the velocity and density.

$$f_i^{(eq)} = \omega_i \rho \left[1 + \frac{c_i \cdot u}{c_s^2 c^2} + \frac{(c_i \cdot u)^2}{2c_s^4} - \frac{u^2}{2c_s^2}\right] \tag{6}$$

For the D3Q19, it can be given as following

$$f_i^{(eq)} = \frac{1}{3}\rho\left[1 - \frac{3}{2}\frac{u^2}{c^2}\right], \qquad i = 0 \tag{7}$$

$$f_i^{(eq)} = \frac{1}{18}\rho\left[1 + 3\frac{c_i \cdot u}{c^2} + \frac{9}{2}\frac{(c_i \cdot u)^2}{c^4} - \frac{3}{2}\frac{u^2}{c^2}\right], \qquad i = 1\sim 6 \tag{8}$$

$$f_i^{(eq)} = \frac{1}{36}\rho\left[1 + 3\frac{c_i \cdot u}{c^2} + \frac{9}{2}\frac{(c_i \cdot u)^2}{c^4} - \frac{3}{2}\frac{u^2}{c^2}\right], \qquad i = 7\sim 18 \tag{9}$$

where ω_i is the weight factor for the i velocity direction, ρ and u are the macroscopic density and velocity, respectively.

It necessary to point out that the Navier-Stokes equations can be recovered in the near-incompressible limit with isotropy, Galilean invariance and a velocity independent pressure from the lattice BGK model through the Chapman-Enskog expansion (Owen et al., 2011; Delbosc et al., 2014) as

$$\frac{\partial \rho}{\partial t} + \nabla \cdot (\rho u) = 0 \tag{10}$$

$$\frac{\partial (\rho u)}{\partial t} + \nabla \cdot (\rho u u) = -\nabla p + \nu (\nabla^2 (\rho u) + \nabla (\nabla \cdot (\rho u))) \tag{11}$$

with an error proportional to O (Ma³) in space and proportional to O (Ma·Δt) in time, where Ma=u/c_s is the Mach number of the system, $p = c_s^2 \rho$ is the pressure, $c_s = c/\sqrt{3}$ is the speed of sound.

2.2. Subgrid turbulence model

In order to model the unresolved scales of motion at high Reynolds numbers, the Smagorinsky model is used to describe the physical effects (Smagorinsky, 1963). This model relates the eddy viscosity to the local strain rate tensor, as follows

$$\nu_{total} = \nu_0 + \nu_t \tag{12}$$

where ν is the total effective viscosity, ν_0 and ν_t are the physical viscosity and eddy viscosity, respectively. The eddy viscosity can be calculated from the local stress tensor

$$\nu_t = C\Delta^2 |\bar{S}| \tag{13}$$

where C is the Smagorinsky constant, Δ is the filter width, and $|\bar{S}|$ is the magnitude of the local stress tensor

$$|\bar{S}| = \sqrt{2\bar{S}_{\alpha\beta}\bar{S}_{\alpha\beta}} \tag{14}$$

$$\bar{S}_{\alpha\beta} = \frac{1}{2}(\frac{\partial \bar{u}_\alpha}{\partial x_\beta} + \frac{\partial \bar{u}_\beta}{\partial x_\alpha}) \tag{15}$$

In the LB method, the fluid viscosity is governed by the relaxation time. So the

eddy viscosity is incorporated into local relaxation time τ_s as

$$\tau_s = 3\nu_{total} + \frac{1}{2} = 3(\nu_0 + C\Delta^2|\bar{S}|) + \frac{1}{2} \qquad (16)$$

The local intensity of the strain tensor is computed from the non-equilibrium momentum flux tensor

$$\bar{\bar{\Pi}}_{\alpha\beta} = \sum_{i=1}^{18} c_{i\alpha}c_{i\beta}(f_i - f_i^{(eq)}) \qquad (17)$$

The solution of the intensity of local stress tensor is:

$$|\bar{S}| = \frac{1}{6C\Delta^2}\left(\sqrt{\nu_0^2 + 18C^2\Delta^2\sqrt{\Pi_{\alpha\beta}\Pi_{\alpha\beta}}} - \nu_0\right) \qquad (18)$$

2.3. Flow configuration

The influence of computational domain size on the time-averaged drag coefficient was previously carried out to obtain the values for unbounded flow. Based on the independency simulation at lower and higher Reynolds numbers, the domain size related to the geometry of 12d × 10d × 10d was found to be adequate in this study. The computational domain is plotted in Fig. 2. The single particle is fixed in the flow domain. The no-slip boundary condition is imposed on the particle surface. In relation to this configuration, a uniform flow with constant velocity is specified at the inlet, and the periodic boundary is imposed at the side walls. The stress-free boundary condition without effect on the flow in the upstream is employed at the outlet. In the present study, the Reynolds number of particle is based on the relative velocity of the fluid with respect to the particle and the kinematic viscosity, which is defined as

$$Re_p = \frac{ud}{\nu} \qquad (19)$$

where u is the averaged fluid velocity through the center of the particle, ν is the

kinematic viscosity, d is the characteristic length. For the non-sphere particle, the diameter of the volume-equivalent sphere is used to define the Reynolds number and the drag coefficient. The hydrodynamic drag force is defined as the parallel component of the combined shear and pressure forces acting on the surface of the immersed particle, as follows

$$F_D = \frac{1}{2} C_D \rho A_p u^2 \tag{20}$$

here C_D is the drag coefficient, A_p is the projected area, and for the non-spherical particle it is calculated with the diameter of the volume-equivalent sphere.
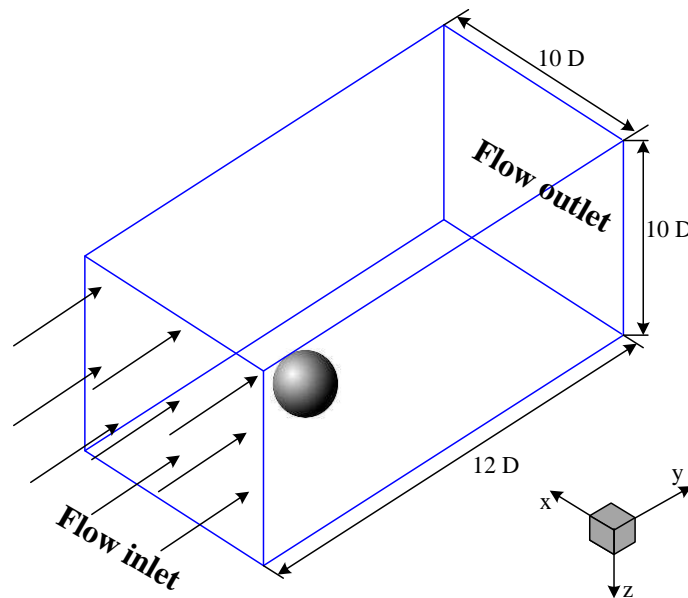

Fig. 2. Computational domain of the flow past a single particle

3. Results and discussion

3.1. Flow past a stationary spherical particle

The resolution of spherical particle is determined by the numbers of lattices for discretizing the diameter of the sphere. As shown in Fig. 3, the particle diameter has a great impact on the particle resolution, which is increased with increasing the particle diameter. The increase in resolution results in a decrease of the sphere roughness, and a smoother sphere is obtained under the higher resolution. Fig. 4 presents the

evolution of drag coefficient at Reynolds numbers (Re$_p$) of 3 and 722. As expected, the flow around the sphere is steady at low Re$_p$, the predicted drag coefficient keeps almost constant after 6000 time steps. With the increase in Re$_p$, the flow will change from steady to unsteady flow. Saha (2004) and Holzer and Sommerfeld (2009) investigated the transition flow from lower Re$_p$ to moderate Re$_p$ for cube and sphere, respectively. At higher Re$_p$ (Re$_p$ = 722), the variation of the drag coefficient is more pronounced with a stronger oscillation, which is derived from the appearance of vortex shedding at higher Re$_p$. Combining the results for both the low and high Re$_p$, the time step from 6000 to 10000 is applied to calculated the time-averaged drag coefficient in the following discussion.
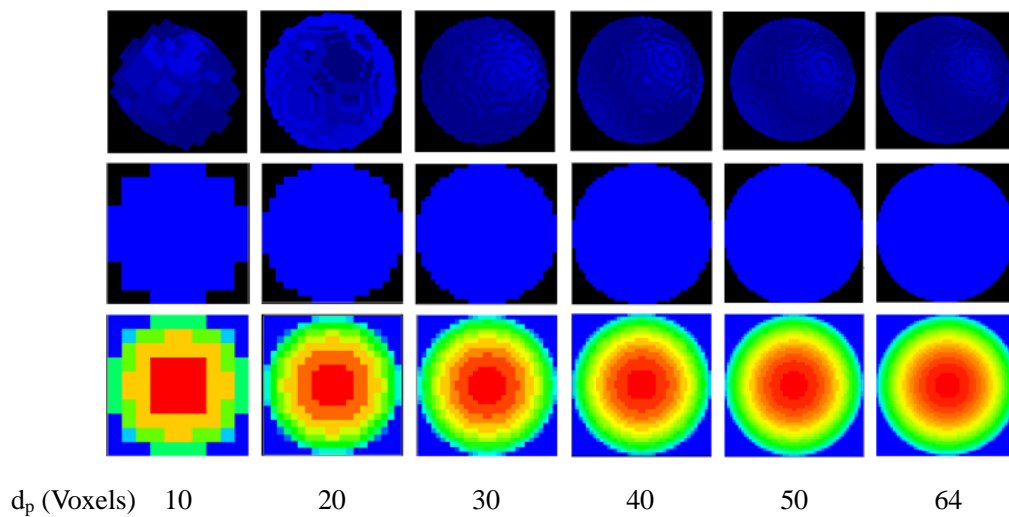

d$_p$ (Voxels)   10   20   30   40   50   64

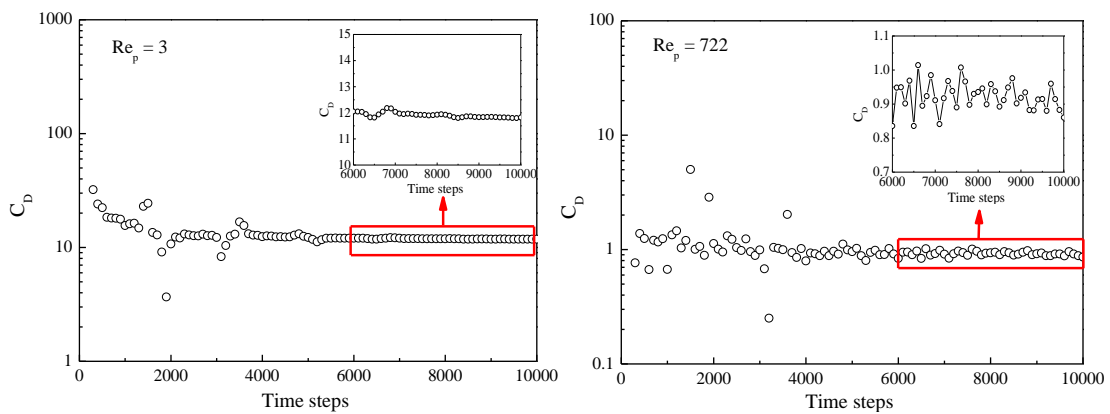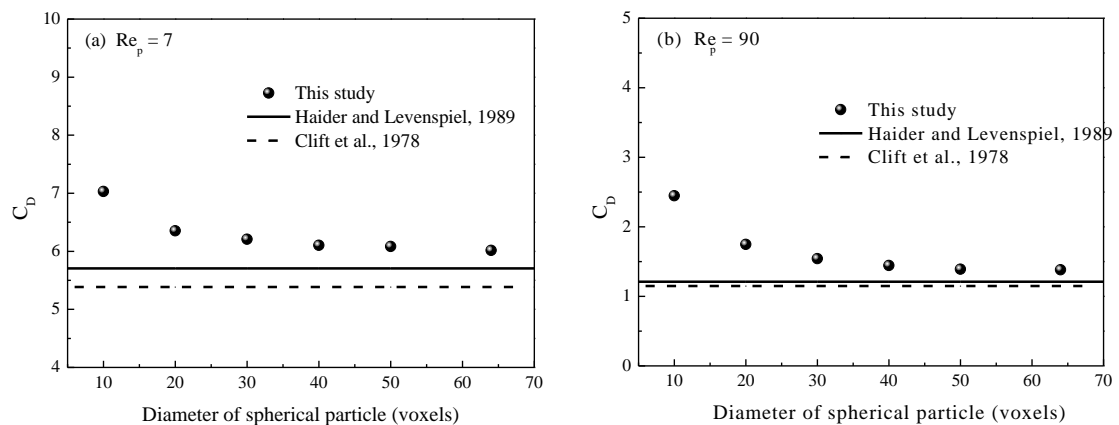**Fig. 3.** Digitization of sphere particle

Fig. 4. Instantaneous behavior of drag coefficient (d$_p$ = 40 voxels)

Fig. 5 exemplarily indicates the time-averaged drag coefficient (C_D) as a function of spherical particle resolution. Here, two well-known correlations are used to verify the predicted ability of digital coupling with Lattice Boltzmann methods, i.e. Clift et al correlation (1978) and Haider and Levenspiel correlation (1989). The correlation of Haider and Levenspiel (1989) was derived from experimental data for spherical, isometric and non-isometric particles in terms of Reynolds number and sphericity, which is calculated as the ratio between the surface area of the volume equivalent sphere and the surface area of the considered particle. Good agreement between the two correlations is obtained, whilst only a small difference observed at the low Re_p. Significant deviations have occurred between the correlation predicted data and the simulated C_D for $d_p = 10$ voxels. With increasing the sphere diameter (particle resolution), the simulated results are tend to close to the correlation predicted data for different Re_p. The difference between the simulated result and correlation prediction increases with the increase in Re_p.
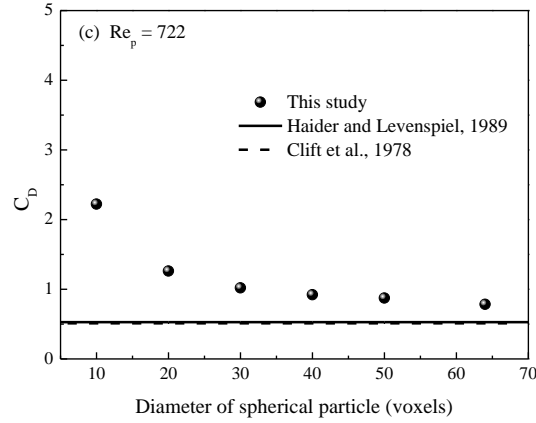
Fig. 5. Effect of particle resolution on the drag coefficient at different Reynolds number

The profiles of time-averaged drag coefficient in a wide range of Reynolds number are plotted in Fig. 6. It is obvious that the C_D is not sensitive with the number of cells for discretizing the sphere diameter at lower Re_p ($Re_p<10$). The simulated results are consistent with the correlation prediction and experimental data. In the current work, the experimental data are corrected from 480-point raw data with eliminating the influence of the wall effect (Brown and Lawler, 2003). When the Re_p is higher than 10, the simulated result is closely dependent on the particle resolution, and the influence of particle resolution on the relative error in C_D increases with increasing the Re_p. Meanwhile, the over prediction of C_D tend to decrease with increasing the particle resolution. Despite the present comparison is only performed in the relevant range of Re_p, as the Re_p continues to increase higher than 1000, the behavior of C_D progressively changes to tend asymptotically towards a constant value under different particle resolutions. The deviations of C_D at the high Re_p are attributed to the decrease in represented resolution along the radial direction of sphere. Therefore, a higher resolution is necessary for the accurate prediction of flow past a
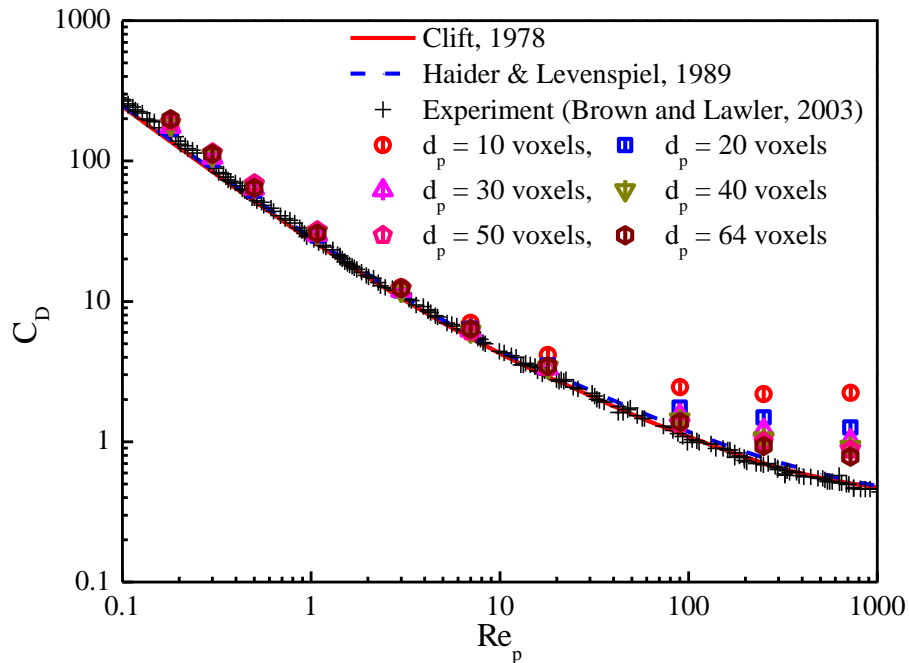
fixed sphere particle at high Re_p.

Fig. 6. Comparison of the drag coefficient of sphere particle against experimental data and empirical correlation

3.2. Flow past a stationary non-spherical particle

The drag force acting on a non-spherical particle is expected to differ from a spherical particle due to its geometrical shape. Three empirical correlations are employed to describe the profiles of non-spherical particle drag coefficient in this study. As can be seen in Figs. 7 and 8, all correlations show a decreasing trend in C_D with increasing Re_p. Different correlations are in good agreement with each other at low Re_p ($Re_p<10$) for both the square cylindrical and cubic particles. For higher Re_p values, C_D becomes less sensitive to the change of Re_p. The minimum C_D is predicted at intermediate Re_p by the the correlations of Haider and Levenspiel (1989) and Ganser (1993), but not by the correlation of Holzer and Sommerfeld (2008).

The predicted profiles for non-spherical particle are similar to that of the spherical

particle. The drag coefficient is slightly higher than that of spherical particle, this trend is more obvious at high Reynolds numbers. Comparison of the numerical results and those from the derived correlations demonstrates the good prediction of C_D at low Re_p for both cubic and cylindrical particles. However, an interesting observation is exhibited in the region from moderate Re_p to high Re_p. The simulated values tend to agree with the correlation of Holzer and Sommerfeld (2008) for cylinder. On the other hand, the difference occurs for the cubic particle, the correlation of Ganser (1993) predicts more accurate drag coefficients before the transform point, whilst Fig.8b shows the good agreement between the numerical results and the prediction of Haider and Levenspiel (1989) after the transform point. This phenomenon is consistent with the finding of Holzer and Sommerfeld (2008). They pointed out that the correlation of Haider and Levenspiel (1989) and Ganser (1993) predict more accurate C_D than that of Holzer and Sommerfeld (2008) correlation for the isometric particle (cube in this study), the mean relative deviations between experimental data and the correlations of Haider and Levenspiel (1989) and Ganser (1993) are approximate 6.5%, while 10.9% for the correlation of Holzer and Sommerfeld (2008). However, for the non-isometric particle (cylinder), the mean relative deviations between the experimental data and the correlations of Haider and Levenspiel (1989) and Ganser (1993) are 42.3% and 32.4%, respectively. A slightly better drag coefficient is predicted by the correlation of Holzer and Sommerfeld (2008) with relative error of 29%. Moreover, it is worth noting that the current resolution for cylinder (L = D = 40 voxels) and cube (L = 40 voxels) produce an accurate and reasonable results. This also implies that the deviation for sphere is largely due to the decrease in resolution in the radial direction for sphere.
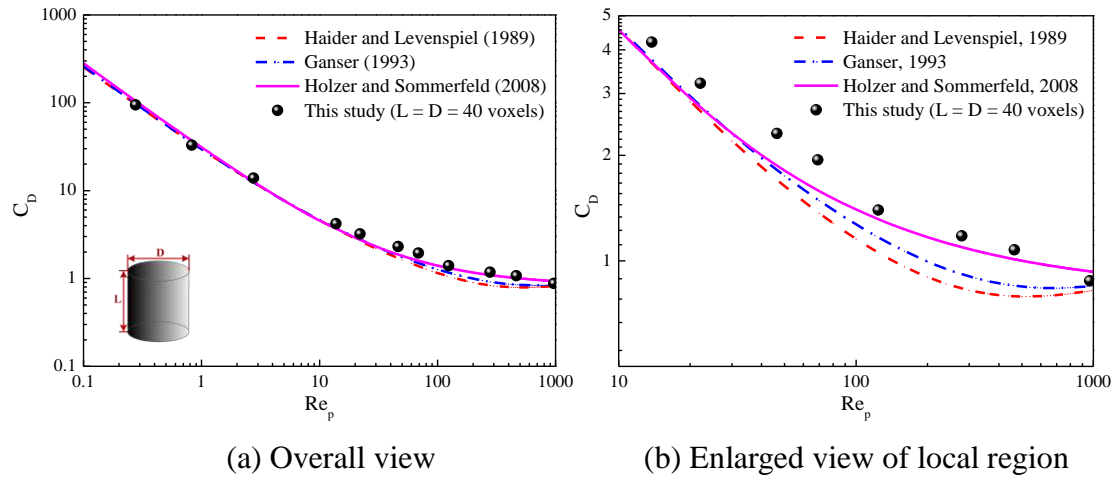
(a) Overall view   (b) Enlarged view of local region

Fig. 7. Comparison of the simulated drag coefficient against empirical correlations
(cylindrical particle)

(a) Overall view   (b) Enlarged view of local region
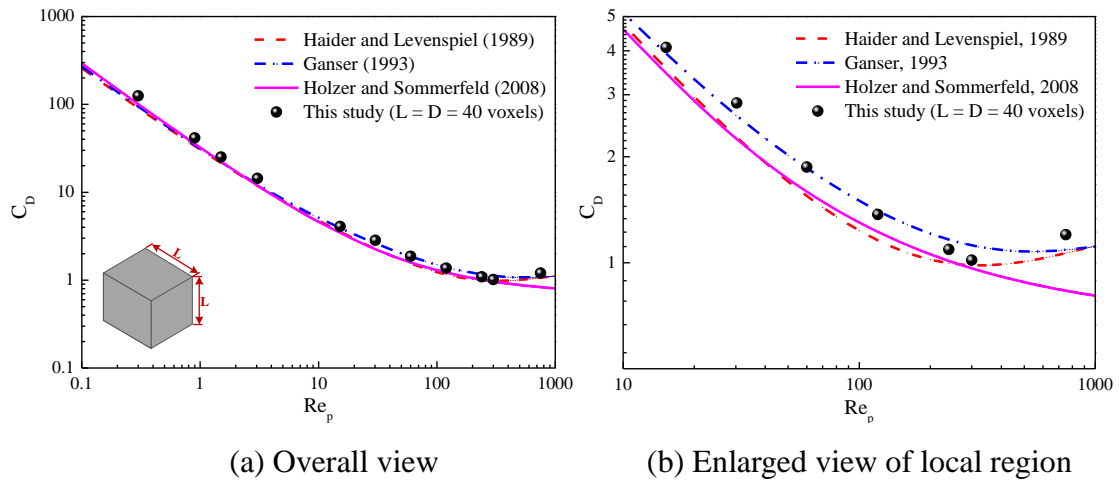
Fig. 8. Comparison of the simulated drag coefficient against empirical correlations
(cubic particle)

4. Conclusions

Flow past a spherical or non-spherical particle has been conducted over a wider range of Reynolds numbers than previously reported. The results have been analyzed and compared with published experimental data and empirical correlations. The main findings can be summarized as follows. The various tests for spherical or non-spherical particle confirm the reliability of the present new computational method, good agreement between the simulated drag coefficient and the experimental date or

empirical correlations is achieved in a wide Reynolds number region. The prediction accuracy for sphere is not sensitive to the resolution at low Reynolds number ($Re_p<10$), but becomes so in the moderate to high Reynolds number range ($10<Re_p<1000$). Moreover, differences in the morphology of non-spherical particles result in different drag coefficient profile, and this becomes more evident with increasing Reynolds number. The simulated drag coefficients for cylindrical particle (non-isometric particle) and cubic particle (isometric particle) are consistent with the empirical correlations, which are established based on a large number of experimental data from the literature. This adds our confidence for the coupling of DigiDEM and LB method for predicting the fluid-particle flow. The next part of the series will focus on ….????????

References

[1] A. Holzer, M. Sommerfeld, Lattice Boltzmann simulations to determine drag, lift and torque acting on non-spherical particles, Comput Fluids 38 (2009) 572-589.

[2] R. Ouchene, M. Khalij, A. Taniere, B. Arcen, Drag, lift and torque coefficients for ellipsoidal particles: From low to moderate particle Reynolds numbers, Comput Fluids 113 (2015) 53-64.

[3] G. Fair, J. Geyer, Water supply and waste water disposal, Wiley, New York, 1954.

[4] A. Haider, O. Levenspiel, Drag coefficient and terminal velocity of spherical and nonspherical particles. Powder Technol. 58 (1989) 63-72.

[5] H. Yow, M. Pitt, A. Salman, Drag correlations for particles of regular shape. Advanced Powder Technol. 16 (2005) 363-372.

[6] P. Brown, D. Lawler, Sphere drag and settling velocity revisited, J. Environ. Eng. 3 (2003) 222-231.

[7] R. Clift, J.R. Grace, M.E. Weber, Bubbles, Drops, and Particles, Academic Press, New York, 1978.

[8] L. Rong, Z. Zhou, A. Yu, Lattice-Boltzmann simulation of fluid through packed beds of uniform ellipsoids, Powder Technol. 285 (2015) 146-156.

[9] A. Holzer, M. Sommerfeld, New simple correlation formula for the drag coefficient of non-spherical particles, Powder Technol. 184 (2008) 361-365.

[10] G. Ganser, A rational approach to drag prediction of spherical and nonspherical particles, Powder Technol. 77 (2008) 143-152.

[11] T. Johnson, V. Patel, Flow past a sphere up to a Reynolds number of 300, J. Fluid Mech. 378 (1999) 19-70.

[12] P. Bagchi, M. Ha, S. Balachandar, Direct numerical simulation of flow and heat transfer from a sphere in a uniform cross-flow, J. Fluid Eng. 123 (2001) 347-358.

[13] G. Atefi, H. Niazmand, M. Meigounpoory, Numerical analysis of 3-D flow past a stationary sphere with slip condition at low and moderate Reynolds numbers, J. Disper. Sci. Technol. 28 (2007) 591-602.

[14] H. Dwyer, D. Dandy, Some influence of particle shape on drag and heat transfer, Phys. Fluids 2 (1990) 2110-2118.

[15] A. Saha, Three-dimensional numerical simulations of the transition of flow past a cube, Phys. Fluids 16 (2004) 1630-1646.

[16] A. Saha, Three-dimensional numerical study of flow and heat transfer from a cube placed in a uniform flow, Int. J. Heat Fluid Flow 26 (2006) 80-94.

[17] A. Vakil, S. Green, Drag and lift coefficients of inclined finite circular cylinders at moderate Reynolds numbers, Comput Fluids 38 (2009) 1771-1781.

[18] A. Richter, P. Nikrityuk, New correlations for heat and fluid flow past ellipsoidal and cubic particles at different angles of attack, Powder Technol. 249 (2013) 463-474.

[19] A. Ladd, Numerical simulations of particulate suspensions via a discretized Boltzmann equation. Part 1. Theoretical foundation, J. Fluid Mech. 271 (1994) 285-309.

[20] A. Ladd, Numerical simulations of particulate suspensions via a discretized Boltzmann equation. Part 2. Numerical results, J. Fluid Mech. 271 (1994) 311-339.

[21] Y. Peng, L. Luo, A comparative study of immersed-boundary and interpolated bounce-back methods in LBE, Prog Comput Fluid Dy 8 (2008) 1-4.

[22] L. Rong, K. Dong, A. Yu, Lattice-Boltzmann simulation of fluid flow through packed beds of uniform spheres: Effect of porosity, Chem. Eng. Sci. 99 (2013) 44-58.

[23] Q. Zhou, L. Fan, Direct numerical simulation of moderate-Reynolds-number flow past arrays of rotating spheres, Phys. Fluids 27 (2015) 073306.

[24] J. Favier, M. Abbaspour-Fard, M. Kremmer, A. Raji, Shape representation of axi-symmetrical, non-spherical particles in discrete element simulation using multi-element model particles, Eng. Comput. 16 (1999) 467-480.

[25] R. Caulkin, X. Jia, C. Xu, M. Fairweather, R. A. Williams, H. Stitt, M. Nijemeisland, S. Aferka, M. Crine, A. Leonard, D. Toye, and P. Marchot, Simulations of structures in packed columns and validation by X-ray tomography, Ind. Eng. Chem. Res., 48 (2009) 202-213.

[26] X. Jia, R.A. Williams, A packing algorithm for particles of arbitrary shapes, Powder Technol. 120 (2001) 175-186.

[27] X. Jia, M. Gan, R.A. Williams, D. Rhodes, Validation of a digital packing algorithm in predicting powder packing densities, Powder Technol. 174 (2007) 10-13.

[28] A. Wachs, L. Girolami, G. Vinay, G. Ferrer, Grains3D, a flexible DEM approach for particles of arbitrary convex shape - Part I: numerical model and validations, Powder Technol. 224 (2012) 374-389.

[29] C. Boon, G. Houlsby, S. Utili, A new contact detection algorithm for three-dimensional non-spherical particles, Powder Technol. 248 (2013) 94-102.

[30] K. Dong, C. Wang, A. Yu, A novel method based on orientation discretization for discrete element modeling of non-spherical particles, Chem. Eng. Sci. 126 (2015) 500-516.

[31] Z. Yu, L. Fan, Lattice Boltzmann method for simulating particle-fluid interactions, Particuology 8 (2010) 539-543.

[32] Q. Li, K. Luo, Q. Kang, Y. He, Q. Chen, Q. Liu, Lattice Boltzmann methods for multiphase flow and phase-change heat transfer, Prog Energ Combust 52 (2016) 62-105.

[33] D. Owen, C. Leonardi, Y. Feng, An effective framework for fluid-structure interaction using the lattice Boltzmann method and immersed moving boundaries, Int. J. Numer. Meth. Engng 87 (2011) 66-95.

[34] N. Delbosc, J. Summers, A. Khan, C. Noakes, Optimized implementation of the Lattice Boltzmann Method on a graphics processing unit towards real-time fluid simulation, Comput. Math. Appl. 67 (2014) 462-475.

[35] J. Smagorinsky, General circulation experiments with the primitive equations, Monthly Weather Review 91 (1963) 99-164.